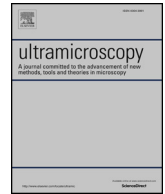




ELSEVIER

Contents lists available at ScienceDirect

Ultramicroscopy

journal homepage: www.elsevier.com/locate/ultramic

Development of analytical ultrafast transmission electron microscopy based on laser-driven Schottky field emission

Chunhui Zhu^a, Dingguo Zheng^{a,b}, Hong Wang^{a,b}, Ming Zhang^a, Zhongwen Li^a, Shuaishuai Sun^a, Peng Xu^a, Huanfang Tian^a, Zian Li^a, Huaixin Yang^{a,b,c,d}, Jianqi Li^{a,b,d,*}^a Beijing National Laboratory for Condensed Matter Physics, Institute of Physics, Chinese Academy of Sciences, Beijing, 100190, China^b School of Physical Sciences, University of Chinese Academy of Sciences, Beijing, 100190, China^c Yangtze River Delta Physics Research Center Co., Ltd., Liyang, Jiangsu, 213300, China^d Songshan Lake Materials Laboratory, Dongguan, Guangdong, 523808, China

ARTICLE INFO

Keywords:

UTEM
Field emission
Ultrafast
Spatiotemporal resolution

ABSTRACT

A new design scheme for ultrafast transmission electron microscopy (UTEM) has been developed based on a Schottky-type field emission gun (FEG) at the Institute of Physics, Chinese Academy of Sciences (IOP CAS). In this UTEM setup, electron pulse emission is achieved by integrating a laser port between the electron gun and the column and the resulting microscope can operate in either continuous or pulsed mode. In pulsed mode, the optimized electron beam properties are an energy width of ~ 0.65 eV, micrometer-scale coherence lengths and sub-picosecond pulse durations. The potential applications of this UTEM, which include electron diffraction, high-resolution imaging, electron energy loss spectroscopy, and photon-induced near-field electron microscopy, are demonstrated using ultrafast electron pulses. Furthermore, we use a nanosecond laser (~ 10 ns) to show that the laser-driven FEG can support high-quality TEM imaging and electron holography when using a stroboscopic configuration. Our results also indicate that FEG-based ultrafast electron sources may enable high-performance analytical UTEM.

1. Introduction

Over the past two decades, we have witnessed substantial progress in the development of ultrafast transmission electron microscopy (UTEM) [1–4]. As a powerful table-top apparatus, UTEM is challenging the resolution abilities of current instruments in both the spatial and temporal domains thanks to well-developed pump-probe and electron microscopy techniques [5–8]. With its nanometer- and sub-picosecond-scale spatiotemporal resolution capabilities, UTEM has enabled visualization of numerous important transient processes, including lattice relaxation [9–11], phase transitions [12–14], nanomechanical motions [15], and the spin [16–18] and electronic dynamics [19–21] of nanoscale materials or structures for studies ranging from physics to chemistry and biology. In addition, the development of UTEM also led to a research direction that fell completely outside the realm of conventional TEM, in the form of photon-induced-near-field electron microscopy (PINEM), a unique experimental technique that can image the light-electron interactions that occur near nanostructures or at an interface and offers exciting prospects for investigation of the dynamics of photonics and plasmonics [22–25].

Because of the extensive application prospects of UTEM, researchers are making major efforts to develop a next-generation high-performance UTEM. One of the major challenges in UTEM development is the lack of high-quality electron emission sources [26]. This limitation also historically hindered the development of conventional TEM and it was solved by the invention of high-performance field emission guns (FEGs), e.g., Schottky-type and cold field emitters [27]. FEGs generally use tip-based emitters that effectively reduce the emitting zone and thus generate electron beams with very high brightness and spatial coherence. Unfortunately, most UTEMs that have been developed to date are based on thermionic electron emission guns [28–34]. These thermionic UTEMs use flat photocathodes with diameters of several tens of microns, thus limiting the performances of the ultrafast electron sources. Therefore, many of the more demanding applications, such as time-resolved electron energy loss spectroscopy (EELS) and electron holography, require the high-performance FEG-based ultrafast electron sources. To the best of our knowledge, only two UTEMs based on FEGs have been implemented, at the University of Göttingen [35, 36] and the University of Toulouse [37,38]. The Göttingen UTEM is based on a Schottky-type FEG, while the Toulouse UTEM uses a cold FEG. Both

* Corresponding author at: Institute of Physics, Chinese Academy of Sciences, 3rd South Street, Zhongguancun, Haidian District, Beijing 100190, China.

E-mail addresses: chunhuizhu@yeah.net (C. Zhu), ljq@aphy.iphy.ac.cn (J. Li).

<https://doi.org/10.1016/j.ultramic.2019.112887>

Received 5 July 2019; Received in revised form 29 October 2019; Accepted 9 November 2019

Available online 10 November 2019

0304-3991/ © 2019 Elsevier B.V. All rights reserved.

instruments show excellent brightness and coherence characteristics in pulsed mode operation [35–38], thus demonstrating the advantages of FEG-based ultrafast electron sources.

In this work, we present another design approach to the development of UTEMs based on Schottky-type FEGs. Our results indicate that FEG-based ultrafast electron sources are suitable for use in the development of high-performance analytical UTEMs. The paper is organized as follows. Section 2 and Section 3 present the details of the proposed setup and its femtosecond electron pulse performances, respectively. In Section 4, the capabilities of the apparatus in the fields of imaging, electron diffraction, EELS, and PINEM are illustrated. In Section 5, using a nanosecond laser, we demonstrate that the FEG-based ultrafast electron sources can support both high-performance TEM imaging and electron holography. Finally, in Section 6, we discuss some of the remaining open questions about the development of UTEM.

2. Instrumentation

Pump-probe configurations: As demonstrated by the pioneering works performed at the Technical University of Berlin [39], the California Institute of Technology (Caltech) [40] and Lawrence Livermore National Laboratory (LLNL) [41], the pump-probe technique is a suitable approach to realize the time resolution required in UTEMs. Within this framework, the evolution of the time-dependent processes is recorded by scanning the time delay between the arrival of the pump and probe pulses, thus enabling a time resolution capability (sub-picosecond) that is approximately 10 orders of magnitude better than that of charge-coupled device (CCD) recordings, thanks to the ultrashort pulse durations of the femtosecond laser sources and the precision of optical delay lines.

The components in the presented UTEM are shown schematically in Fig. 1. The main laser source is an Yb:KGW integrated laser system called Pharos (Light Conversion Inc.). This system emits ~ 190 fs pulses, which are centered at $\lambda = 1030$ nm, with an average power ranging up to 10 W and a tunable repetition rate that ranges from a single shot to 1 MHz. The laser output is split into two pulses using an 80/20 beam splitter; the low-intensity beam is directed toward a delay line after fourth-harmonic generation (~ 257 nm) using beta barium borate (BBO) crystals and is then focused on the TEM cathode to generate probing electron pulses; the high-intensity beam is focused onto the sample, either after second-harmonic generation (~ 515 nm) using a BBO crystal or after passing through a collinear optical parametric amplifier (OPA) system (Orpheus-HP, Light Conversion Inc.), to trigger the nonequilibrium state in the sample. The OPA system operates at a repetition

rate of 200 kHz and provides laser pulses with wavelengths ranging from 210 nm to 16 μm . The sizes of the laser beam spots on the cathode and the sample are ~ 60 μm and ~ 40 μm , respectively. In addition, we also integrated a 10 kHz, 355 nm nanosecond laser (~ 10 ns pulse duration) into the probing laser path. Notably, several motorized flippers (Thorlabs Inc.) are present in the optical paths. These flippers enable program-controlled changes of the laser source.

TEM modification: Fig. 2a shows a photograph of the proposed UTEM apparatus. This apparatus is based on a commercial JEOL 2100F TEM with a 200 kV Schottky-type FEG that uses a ZrO/W nanotip as its cathode. Previously, there were two ways to realize laser-driven field emission sources. The Göttingen group used side illumination through the side window on the TEM gun [35, 36], while the Toulouse group focused a femtosecond laser tightly on the emitter tip using optical components that were integrated inside a cold field emission source [37,38]. Here, we present another approach where optical access to the cathode is achieved by integration of a laser port between the FEG and the column. To this end, we first fabricated a 10-cm-thick stainless steel (or brass) spacer that contained a 45° mirror and an additional vacuum pumping system with vacuum ports for diagnostics. A hole was drilled through the mirror's center to allow the electron beam to pass through, as illustrated in Fig. 2b. In addition, the acceptance apertures in the condenser lens system and the fixed apertures in the anode for the field emission gun have been either removed or modified to produce a higher beam exiting from the accelerator into the UTEM condenser lens. Although this modification was developed for the purposes of ultrafast imaging and visualization of lattice dynamics, it is also confirmed that a TEM with this type of modification can be used appropriately to perform conventional TEM investigations with high spatial resolution, as discussed in the following. Furthermore, the proposed design scheme also enables easy replacement of the electron gun. Because no optical devices are mounted on electron gun, it is possible to change the electron gun by following the original procedure (both the customized electron gun and the replacement procedure can be obtained from the manufacturer) and then looking rapidly at the photoemission state of the UTEM. Refinement of the positioning of the lens that focuses the probing laser on the emitter is usually necessary, but this process can be completed in an hour by an experienced engineer or staff member. The pump beam is directed toward the sample using the port that is usually reserved for energy-dispersive X-ray spectrometry. The apparatus is equipped with a Gatan spectrometer (GIF 965) for EELS and energy filtered transmission electron microscopy (EFTEM).

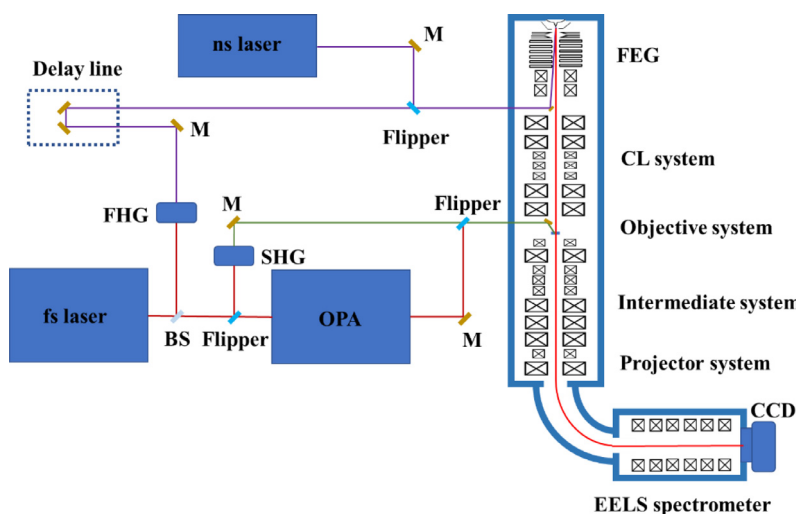


Fig. 1. Conceptual design of UTEM instrument at IOP CAS. OPA: optical parametric amplifier; BS: beam splitter; M: mirror; SHG: second harmonic generation; FHG: fourth harmonic generation; FEG: field emission gun; CL: condenser lens; EELS: electron energy loss spectroscopy; CCD: charge-coupled device.

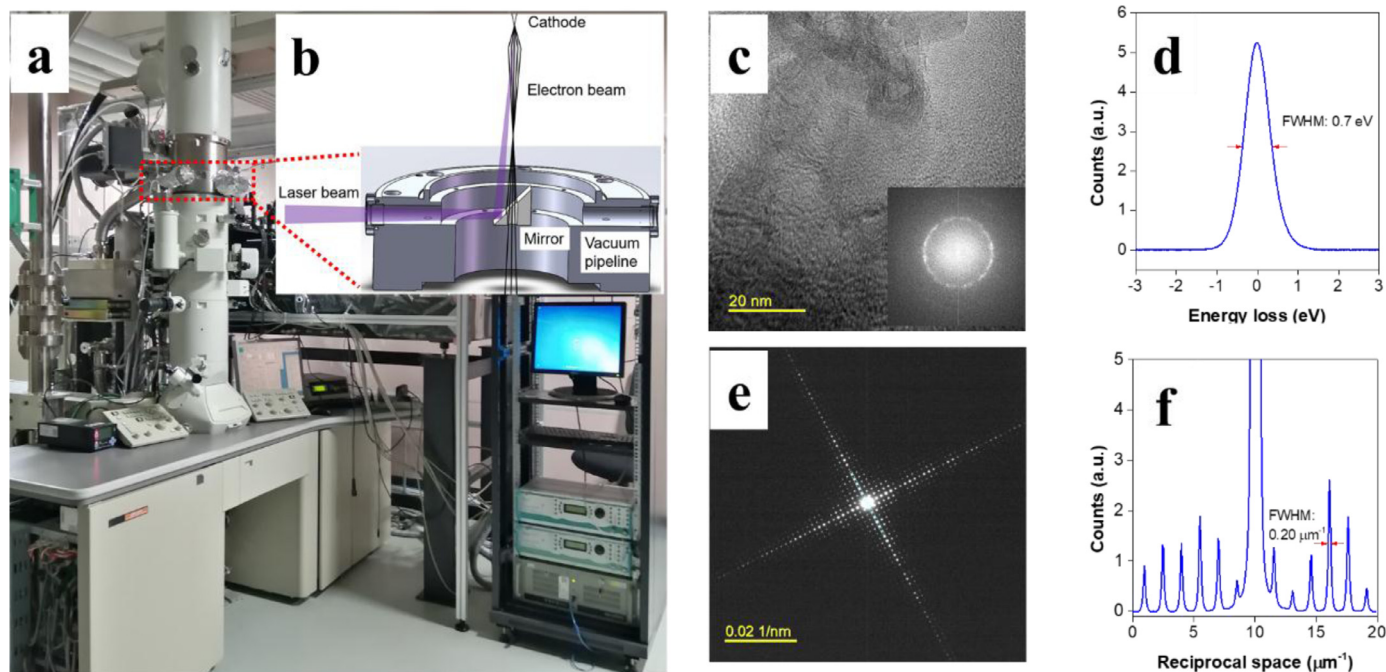


Fig. 2. UTEM apparatus and its performance in continuous mode. (a) Photograph of the instrument. (b) Schematic diagram of the laser port. (c) HRTEM image of carbon black; its Fourier transform is shown in the inset. (d) Zero-loss peak (ZLP) of EELS. (e) High-dispersion diffraction (HRD) pattern of the 500 nm grating and (f) its profile.

3. UTEM operation and performances

Continuous mode: After modification, the proposed instrument can operate in both continuous and pulsed modes. We focus initially on continuous mode operation here. Fig. 2c shows a high-resolution TEM (HRTEM) image of a carbon black sample. The lattice fringes at approximately 0.34 nm are clearly visible. As shown in Fig. 2d, the full width at half maximum (FWHM) value of the zero-loss peak (ZLP) in EELS is ~ 0.7 eV, thus revealing the energy resolution of the apparatus when operating in continuous mode. Fig. 2e presents a high-dispersion diffraction (HRD) pattern that was obtained from a 500-nm-spaced grating replica. The FWHM of this pattern's diffraction spots is approximately $0.20 \mu\text{m}^{-1}$ (Fig. 2f), which yields a transverse coherence length of $\sim 2.1 \mu\text{m}$. Notably, the factor $\alpha_{\text{FWHM}} = 2(2\ln 2)^{1/2}\sigma_{\alpha} \approx 2.35\sigma_{\alpha}$ has been applied to transform a FWHM value into a standard deviation. These results indicate that the modification of the TEM apparatus has had a negligible impact on its continuous mode performance.

Pulsed mode: We now focus on the photoemission beam qualities of the laser-driven FEGs. Two FEGs are characterized here. Gun-1 has been used for nearly six months and Gun-2 has been used for approximately four years. Fig. 3 shows a series of results that were obtained from Gun-1 using Pharos, which operated at a repetition rate of 1 MHz. The beam profile of the electron pulses acquired with magnification (Mag.) of $30k\times$ is presented in Fig. 3a. The profile has a Gaussian shape with FWHM of ~ 3.55 nm (Fig. 3b). An HRD pattern and its pulsed mode profile are shown in Figs. 3b and 3c, respectively, giving a transverse coherence length of $\sim 0.7 \mu\text{m}$. The energy width for the photoemitted pulsed electron is approximately 0.65 eV, as shown in Fig. 3d. This width is comparable to that obtained when using the setup in continuous mode. These results indicate that the performance levels of the proposed setup are similar to those of other FEG-based UTEM systems, e.g., the UTEM in Göttingen (~ 0.6 eV energy width and micron-scale coherence length) and the UTEM in Toulouse (~ 1 eV energy width) [35–38].

In a FEG-based TEM, several parameters, including the extraction potentials (A1, A2), the suppressor voltage (Bias) and the filament current, can be used to control the electron beam properties. In

continuous mode, A1, A2, the Bias and the filament current for this FEG are fixed at 3.2 kV, 7.8 kV, 0.3 kV and 2.15 A, respectively. In pulsed mode, the filament current and/or A1 are reduced to suppress static electron emissions. The A1 and filament current values used are usually in the ranges of 2.5–3.2 kV and 1.3–1.8 A (corresponding to an emitter temperature range of ~ 1100 – 1500 K). The electrical field shape near the emitter of the Schottky-type FEG can be described using a dimensionless parameter [42]:

$$\Gamma = \frac{U_{\text{tip}} - U_{\text{sup}}}{U_{\text{ext}} - U_{\text{sup}}} \cdot \frac{d_{\text{ext-sup}}}{d_{\text{tip-sup}}}$$

where U_{tip} , U_{sup} , U_{ext} , $d_{\text{ext-sup}}$ and $d_{\text{tip-sup}}$ are the tip voltage, the suppressor voltage, the extractor voltage, the extractor-suppressor distance and the tip-suppressor distance, respectively. When Bias = 0, Γ is equal to 0. An increasing Bias value (i.e., increasing Γ) can lead to focusing behavior for the electrode assembly and results in an increased electron dose in the sample plane. For A1 = 2.5 kV and A2 = 7.8 kV, an increase in the photoemission current of $\sim 20\%$ is found as Bias increases from 0 to 0.3 kV. However, the extractor voltage-dependent behavior is rather complex. When A1 decreases from 3.2 kV to 0.55 kV, the photoemission current initially decreases and then begins to increase at a critical voltage of ~ 1 kV before beginning to decrease again at ~ 0.62 kV, as shown in Fig. 4a. This complex behavior probably occurs because A1 is not only related to the electric extraction field, but also creates an electrostatic lens system in combination with A2.

The laser power-dependent photocurrents were measured under given illumination conditions, i.e., Mag. $2000\times$, spot size 1, alpha 3, A1 = 2.5 kV, A2 = 7.8 kV, Bias = 0.3 kV and filament current = 1.8 A. At a laser power of ~ 20 mW, we obtained ~ 33 camera counts per pulse, corresponding to a photocurrent of ~ 1.32 pA for 1 MHz operation. The photoemission current increased linearly with increasing laser power over the entire measurement range (Fig. 4b), but strong degradation of the beam's properties has been already observed at this laser power. No further increases in the laser power are planned with the aim of protecting the emitter (and increasing its service life). The laser polarization-dependent photoemission current is shown in Fig. 4c. In contrast to the side illumination mode, which exhibited strong polarization-

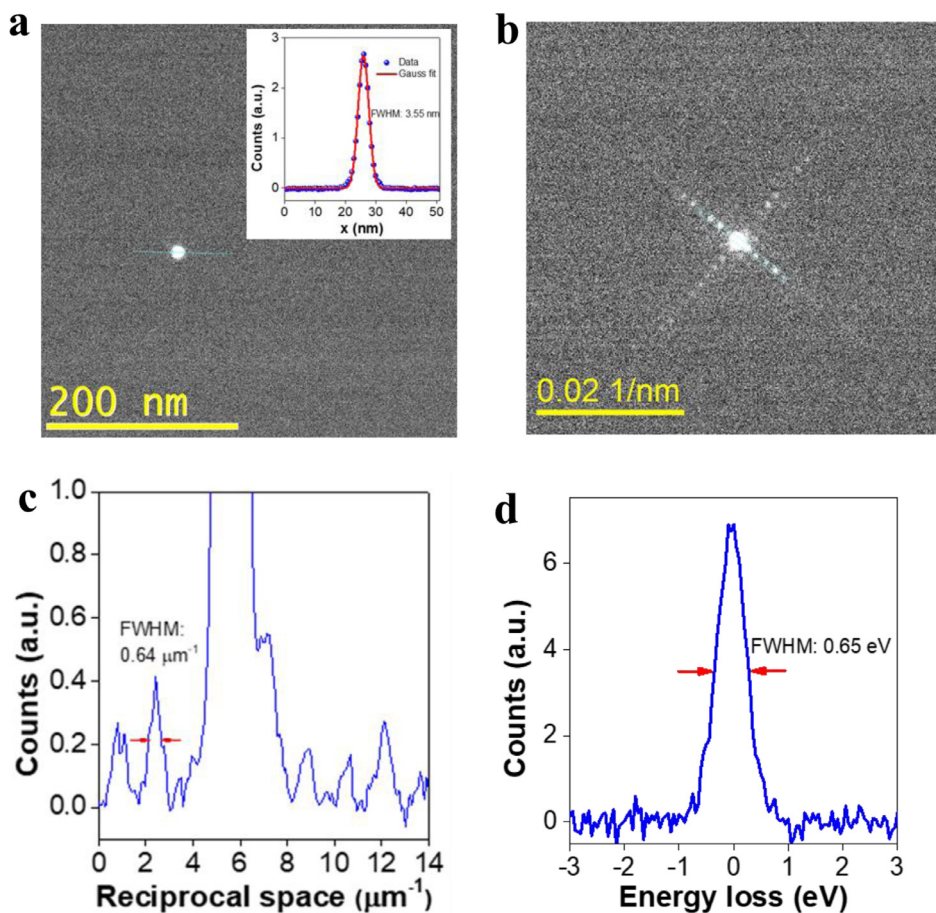


Fig. 3. Electron pulse properties of UTEM apparatus. (a) Image of the pulsed electron beam and its profile (inset). (b) HRD of a 500 nm grating and (c) its profile. (d) ZLP of EELS in pulsed mode.

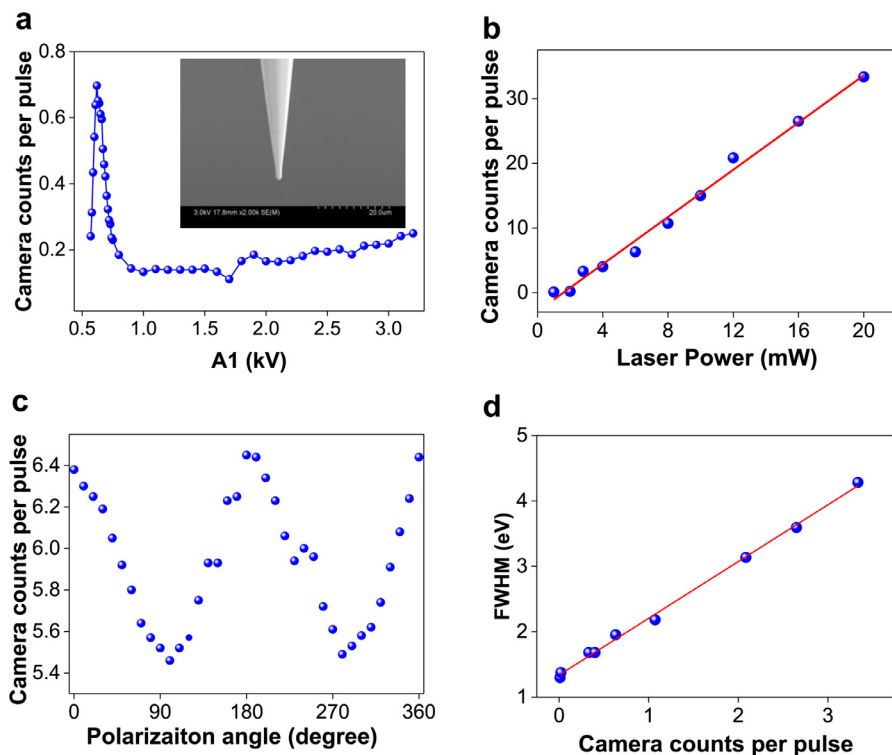


Fig. 4. Dependence of electron pulse properties on experimental conditions. (a) Camera counts per pulse as a function of A1 (A2 = 7.8 kV, filament current = 1.3 A, laser power = 1 mW). The inset shows an SEM image of the emitter after UTEM operation of ~1 year. (b) Camera counts per pulse as a function of incident laser power (A1 = 2.5 kV, A2 = 7.8 kV, filament current = 1.8 A). (c) Polarization-dependent photoemission counts (A1 = 2.5 kV, A2 = 7.8 kV, filament current = 1.6 A, laser power = 4.8 mW). (d) Dependence of FWHM of ZLP on number of camera counts in each pulse. The red line corresponds to a linear fit to guide the eye. For all measurements in this figure, spot size 1 and alpha 3 were used.

Table 1

Properties achieved by thermionic and FEG-based UTEMs in our laboratory. Spot size 1 and alpha 3 were used during data acquisition.

	Source type ^a	Cathode material	Accelerating voltage	Energy width ^b	Coherence length ^c	Lattice resolution	Pulse duration	Counts per pulse ^d
1	thermionic gun-fs	LaB ₆	160 keV	–	1.3 μm	0.34 nm	<1 ps	~5000
2	Gun-1-fs	ZrO/W	200 keV	0.65 eV	0.7 μm	0.34 nm	<1 ps	~33
3	Gun-1-ns	ZrO/W	200 keV	0.62 eV	1.6 μm	0.34 nm	>10 ns	~8000
4	Gun-2-fs	ZrO/W	200 keV	1.8 eV	0.6 μm	0.34 nm	<1 ps	~18
5	Gun-2-ns	ZrO/W	200 keV	1.8 eV	1.6 μm	0.34 nm	>10 ns	~5000

^a The photoemission is driven by a 200 kHz, 300 fs pulsed laser for the thermionic gun, a 1 MHz, 190 fs pulsed laser for the FEGs in femtosecond mode, and a 10 kHz, 10 ns pulsed laser for the FEGs in nanosecond mode.

^b For energy resolution measurements, the electron beam diameter was set at ~2 μm and the laser power was fixed at 1 mW.

^c The coherence length was obtained from high-dispersion diffraction measurements on a 500 nm spaced grating replica with an electron beam diameter of ~50 μm. The laser power was fixed at 20 mW for the femtosecond mode and 100 mW for the nanosecond mode.

^d The used laser conditions were the same as those used for the coherence length measurements.

dependent behavior [36–38], the maximum current difference (less than ~17%) obtained from a different polarization state is much smaller when using this geometry. The polarization-dependent current can possibly be attributed to the fact that the incident laser beam is not exactly perpendicular to the emitter front facet. An angle of incidence of a few degrees may exist that is caused by either the laser alignment (Fig. 2b) or the curvature of the nano-tip surface.

In addition to the photoemission current, the other electron beam characteristics (e.g., energy monochromaticity, coherence length) are also sensitive to these parameters, particularly when space charge effects occur [36, 41]. Therefore, it is necessary to make a trade-off to obtain high quality experimental data and it is also essential to be careful when changing the photoemission conditions to prevent any change from affecting the accuracy of the results. For example, the energy resolution of EELS may deteriorate obviously when the pulses contain large numbers of electrons (Fig. 4d).

In pulsed mode, Gun-2 shows the same trends with variations of the extraction potential, the suppressor voltage, the filament current and the laser power, although it does show different parameters for given conditions (see Table 1). It should be noted that two peaks can be observed in the ZLP of EELS for Gun-2 in pulsed mode, although only one peak exists in the continuous mode. This happens because the ZrO coating on the emitter is close to depletion after usage of approximately four years and thus both ZrO and W make contributions to the photoemission. We also operated the system in nanosecond mode for both FEGs and the parameters obtained are listed in Table 1. The emitter of Gun-2 was checked after UTEM operation for ~1 year (~10 months in femtosecond mode and ~2 months in nanosecond mode). As shown in the inset of Fig. 4a, no significant change was observed, except that the tip is thicker than recommended by the manufacturer (~300 nm).

Electron pulse duration: To obtain the electron pulse duration for the proposed instrument, we performed PINEM experiments on the edge of the Cu-grid by following the work of Liu et al. [23]; the temporal duration of the PINEM effect involves a cross-correlation between the laser pulses and the electron pulses due to the short lifetimes of the photo-induced surface charge density waves. Fig. 5a shows the time and energy dependences of the PINEM electron energy spectra. At time zero (0 ps), the energy spectrum represents a series of loss and gain peaks that occur at integer multiples of the photon energy due to the absorption and emission of photons associated with the near-field interaction. The temporal evolutions of the ZLP and the $\pm 3\hbar\omega$ satellite peaks are illustrated in Fig. 5b. The pulse duration τ_{FWHM} is assigned to the FWHM that was obtained from a Gaussian fitting. As shown in Fig. 5c, this duration decreases from ~704 fs to ~405 fs as the peak order n increases from 1 to 5, with a relationship given by $\tau_{\text{FWHM}} \propto \frac{1}{\sqrt{|n|}}$ (see Fig. 5d). The temporal narrowing can be attributed to the fact that the higher-order energy gain/loss is nonlinearly dependent on the excitation pulse intensity. A detailed theoretical study invoking higher-order Bessel functions may allow a quantitative understanding of this nonlinear behavior [43] but is beyond the scope of the current study. In

addition, a chirp of ~286 fs/eV was estimated from Fig. 5a. Notably, the PINEM experiment not only demonstrated a sub-picosecond electron pulse duration but also gave exemplary time-resolved experimental results and demonstrated the capability of our setup for investigation of photo-induced near-field effects around the nanostructures.

4. Potential applications

Electron diffraction and HRTEM imaging are the two fundamental functions of TEM. These functions provide valuable crystal structure information. Several important lattice dynamic processes (e.g., the phase transition in VO₂ and the electron–phonon coupling in carbon nanotubes) have been revealed through analysis of electron diffraction data that were obtained via either UTEM or ultrafast electron diffraction (UED) [9–14]. To demonstrate the diffraction capability of the proposed apparatus, we performed selected area electron diffraction (SAED) experiments on a ZrSiS sample in pulsed mode. As shown in Fig. 6a, a high signal-to-noise ratio was obtained for the SAED pattern. The best recorded HRTEM imaging resolution that has been achieved is 0.34 nm for a sample composed of carbon nanotubes, as shown in Fig. 6b. It should be noted here that the HRTEM resolution is highly sensitive to the experimental conditions, e.g., the electron dose per pulse and the thermal drift of the specimen [26]. In general cases, the spatial resolution for pulsed mode operation is approximately 1 nm. The ultimate lattice imaging resolution that was obtained by the Toulouse UTEM was ~0.9 nm [38]. Although direct visualization of the lattice dynamics via HRTEM imaging seems to be impossible until the thermal drift problem is resolved, the results presented here demonstrate that the quality of the ultrashort electron pulses generated using a FEG-based photoemission electron gun can support HRTEM imaging in the parallel illumination mode. In the next Section, using a nanosecond laser, we will further clarify the intrinsic imaging capabilities of the FEG-based UTEM.

Lorentz TEM is a powerful technique that has been used to perform quantitative analysis of magnetic domain structures on the nanoscale [44]. This technique has been used to image and analyze complex magnetic textures, such as magnetic skyrmions with spatial resolution of 2 nm, and to visualize the flux vortex lattices in Type II superconductors [45, 46]. The proposed UTEM has been operated successfully in Lorentz mode. An example experiment was performed on a PbFe₁₂O₁₉ sample. In Fig. 6c, the nanoscale magnetic structures are shown clearly and distinctly. By combining Lorentz TEM with different pump-probe configurations, a number of magnetic dynamics, e.g. martensitic transitions and nucleation, can be revealed directly in real space with sub-picosecond time resolution [4].

EELS analyzes the energy distributions of electrons after they pass through a sample. These energy distributions are a rich source of information about the electronic structures of the sample. To explore the potential of time-resolved EELS, we present the low-loss and core-loss

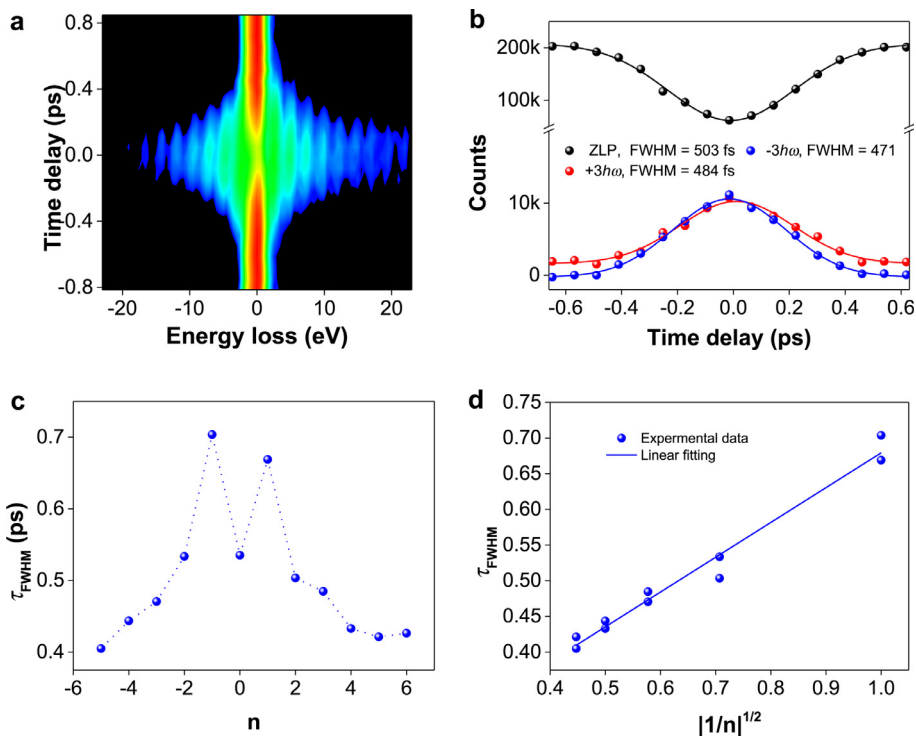


Fig. 5. PINEM spectra and their temporal resolution. (a) Time and energy dependences of PINEM spectra. (b) Temporal evolution of the ZLP and $\pm 3\hbar\omega$ satellite peaks. (c) FWHM as a function of the peak order. (d) τ_{FWHM} vs. $\frac{1}{\sqrt{|n|}}$, showing a linear relationship.

EELS of carbon nanotubes in Fig. 7a and 7b, respectively. The low-loss region occurs near the ZLP and contains information about the interactions of the valence electrons and the bulk and surface plasmons. The core-loss region in Fig. 7b is related to the K-shell electron excitation of carbon. PINEM extends the energy spectroscopy experiments to the regime of probing the evanescent near-field that surrounds the nanostructures [22–25]. In Fig. 7c, we present an image of a silver nanowire at the time zero using the electrons from the four gain peaks (inset of Fig. 7c). The surface plasmon polariton standing wave around the nanowire is clearly visible, thus demonstrating the prospects of the technique for investigation of light-electron interactions [24].

5. Imaging and holography in nanosecond mode

Because of the cathode geometry, the maximum numbers of photoemission electrons that can be generated using FEG-based ultrafast electron sources are limited [38, 47]. Very long exposure times (of tens of seconds or more) are usually required, thus challenging the mechanical stability of the UTEM. Furthermore, strong space-charge effects are inevitable when high photoemission electron densities are formed near the tip emitter within a sub-picosecond period [36].

Therefore, to illustrate the intrinsic imaging capabilities of the FEG-based UTEM, we perform nanosecond stroboscopic experiments to avoid the deleterious effects of both sample drift and Coulomb interactions. In this case, a 10 kHz, 355 nm nanosecond laser and Gun-2 are used. As shown in Fig. 8a and 8b, the HRTEM imaging quality has improved greatly when compared with that obtained using the femtosecond lasers (Fig. 6b). The lattice fringes of the carbon crystal shown in Fig. 8a become apparent. As a further exploration of the potential of our setup, an electron hologram is acquired with a biprism voltage of ~ 40 V. As shown in Fig. 8c and 8d, the electron hologram shows a field of view of 2–3 μm and good fringe contrast. Pulsed electron holography experiments on Fe nanowires are currently in progress and will be the subject of a forthcoming publication.

6. Discussion

Table 1 summarizes the electron pulse properties that were obtained from the thermionic and FEG-based UTEMs in our lab. The thermionic UTEM is based on the JEOL-2000EX TEM and the details of this setup were reported in [9]. The results show that, when using femtosecond electron pulses, both instruments show similar coherence lengths and

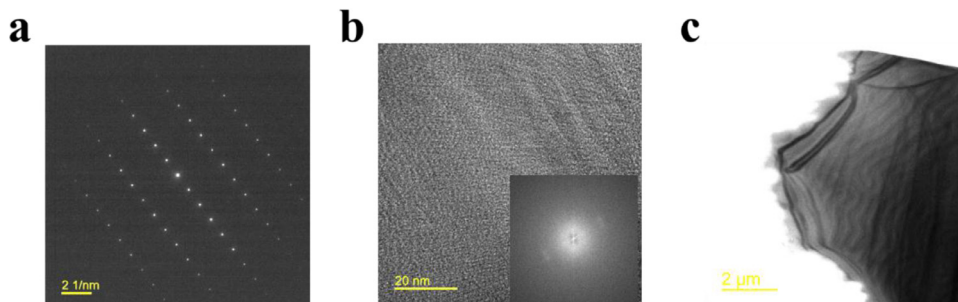


Fig. 6. Electron diffraction and imaging in pulsed mode. (a) Electron diffraction pattern for ZrSiS sample (binning 2, exposure time 5 s). (b) HRTEM image of carbon nanotubes and its Fourier transform (binning 1, exposure time 20 s). (c) Lorentz image of PbFe₁₂O₁₉ sample (binning 1, exposure time 120 s).

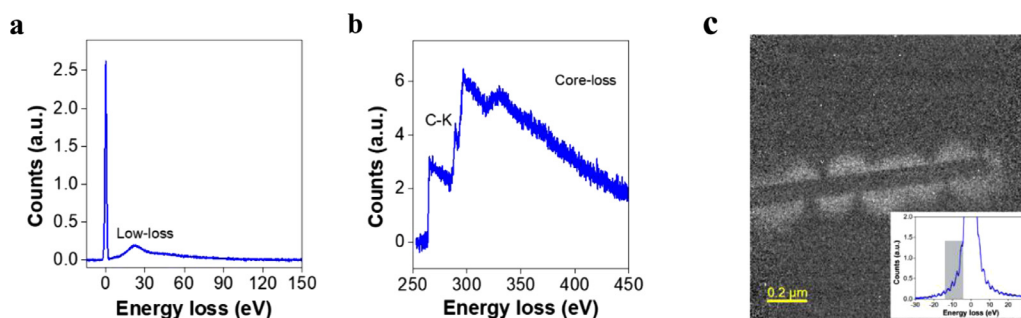


Fig. 7. EELS and PINEM imaging in pulsed mode. (a) Low-loss and (b) core-loss EELS for carbon nanotubes. (c) PINEM image obtained from silver nanowires with four gain peaks, as shown in the inset (binning 8, exposure time 100 s).

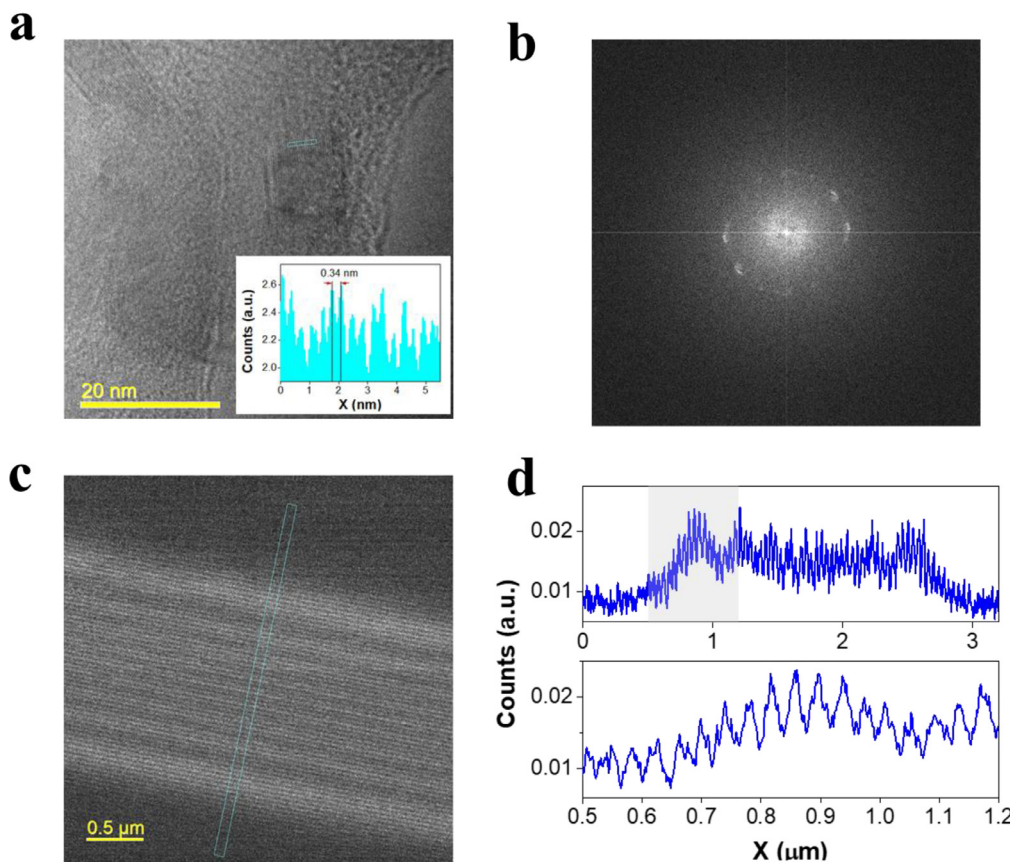


Fig. 8. HRTEM image and electron hologram obtained using nanosecond laser and Gun-2. (a) HRTEM image of carbon black (binning 1, exposure time 20 s), and (b) its Fourier transform. (c) Pulsed mode electron hologram and (d) its profile (binning 1, exposure time 10 s). The bottom panel in (d) is an expanded view of part of the upper panel.

lattice resolutions. In other words, until now, we cannot determine distinct advantages for the FEG-based UTEM for femtosecond imaging applications. However, as demonstrated using the nanosecond laser, the FEG-based UTEM has the potential to be improved if the space-charge effects and sample drift problems can be solved. More importantly, the FEG-based UTEM enables high quality EELS analysis with energy resolution that is much better than that of the thermionic UTEM (1–2 eV) and it also enables another very useful function in the form of electron holography. These aspects are beneficial to the development of a high-performance analytical UTEM.

In conclusion, we have presented a method to develop field-emission ultrafast transmission electron microscopy based on the use of Schottky-type FEGs. The proposed setup enables sub-picosecond electron pulses to be produced with an energy width of 0.65 eV and micrometer-scale spatial coherence length, and the proposed setup can operate in imaging, diffraction, EELS, PINEM and electron holography modes. We also demonstrate that the FEG-based ultrafast electron sources are suitable for use in development of an analytical UTEM. To

enable further improvements in the instrumental performances, research should focus on the space-charge effects, the mechanical stability of the TEM and the signal-to-noise ratio of the CCD camera.

Declaration of competing interest

The authors declare that they have no known competing financial interests or personal relationships that could have appeared to influence the work reported in this paper.

Acknowledgments

Funding: This work was supported by the National Key Research and Development Program of China [grant numbers 2016YFA0300303, 2017YFA0504703, 2017YFA0302904, 2017YFA0303000]; the National Natural Science Foundation of China [grant numbers 11774391, 11774403, 11804381]; the Strategic Priority Research Program (B) of the Chinese Academy of Sciences [grant numbers XDB25000000,

XDB07020000]; the Scientific Instrument Developing Project of the Chinese Academy of Sciences [grant number ZDKYYQ20170002]; and the China Postdoctoral Science Foundation funded project [grant number BX20180351]. We thank David MacDonald, MSc, from Liwen Bianji, Edanz Editing China (www.liwenbianji.cn/ac), for editing the English text of a draft of this manuscript.

Supplementary materials

Supplementary material associated with this article can be found, in the online version, at [doi:10.1016/j.ultramic.2019.112887](https://doi.org/10.1016/j.ultramic.2019.112887).

References

- [1] A.H. Zewail, Four-dimensional electron microscopy, *Science* 328 (2010) 187–193, <https://doi.org/10.1126/science.1166135>.
- [2] N.D. Browning, G.H. Campbell, J.E. Evans, T.B. LaGrange, B.W. Reed, Electron microscopy and spectroscopy on the ultrafast timescale, *Chem. Phys. Chem.* 11 (2010) 781–782, <https://doi.org/10.1002/cphc.200900937>.
- [3] A. Adhikari, J.K. Eliason, J. Sun, R. Bose, D.J. Flannigan, O.F. Mohammed, Four-dimensional ultrafast electron microscopy: insights into an emerging technique, *ACS Appl. Mater. Interfaces* 9 (2017) 3–16, <https://doi.org/10.1021/acsmi.6b12301>.
- [4] H.X. Yang, S.S. Sun, M. Zhang, Z.W. Li, Z.A. Li, P. Xu, H.F. Tian, J.Q. Li, Ultrafast electron microscopy in material science, *Chin. Phys. B* 27 (2018) 070703, <https://doi.org/10.1088/1674-1056/27/7/070703>.
- [5] P. Baum, A.H. Zewail, Attosecond electron pulses for 4D diffraction and microscopy, *PNAS* 104 (2007) 18409–18414, <https://doi.org/10.1073/pnas.0709019104>.
- [6] K.E. Priebe, C. Rathje, S.V. Yalunin, T. Hohage, A. Feist, S. Schäfer, C. Ropers, Attosecond electron pulse trains and quantum state reconstruction in ultrafast transmission electron microscopy, *Nat. Photonics* 11 (2017) 793–797, <https://doi.org/10.1038/s41566-017-0045-8>.
- [7] Y. Morimoto, P. Baum, Diffraction and microscopy with attosecond electron pulse trains, *Nat. Phys.* 14 (2018) 252–256, <https://doi.org/10.1038/s41567-017-0007-6>.
- [8] G.M. Vanacore, I. Madan, G. Berruto, K. Wang, E. Pomarico, R.J. Lamb, D. McGrouther, I. Kaminer, B. Barwick, F.J.G. de Abajo, F. Carbone, Attosecond coherent control of free-electron wave functions using semi-infinite light fields, *Nat. Commun.* 9 (2018) 2694, <https://doi.org/10.1038/s41467-018-05021-x>.
- [9] G.L. Cao, S.S. Sun, Z.W. Li, H.F. Tian, H.X. Yang, J.Q. Li, Clocking the anisotropic lattice dynamics of multi-walled carbon nanotubes by four-dimensional ultrafast transmission electron microscopy, *Sci. Rep.* 5 (2015) 8404, <https://doi.org/10.1038/srep08404>.
- [10] J. Hu, G.M. Vanacore, A. Cepellotti, N. Marzari, A.H. Zewail, Rippling ultrafast dynamics of suspended 2D monolayers, graphene, *PNAS* 113 (2016) E6555–E6561, <https://doi.org/10.1073/pnas.1613818113>.
- [11] A.J. McKenna, J.K. Eliason, D.J. Flannigan, Spatiotemporal evolution of coherent elastic strain waves in a single MoS₂ flake, *Nano Lett.* 17 (2017) 3952–3958, <https://doi.org/10.1021/acs.nanolett.7b01565>.
- [12] M.S. Grinolds, V.A. Lobastov, J. Weissenrieder, A.H. Zewail, Four-dimensional ultrafast electron microscopy of phase transitions, 103 (2006) 18427–18431, 10.1073/pnas.0609233103.
- [13] R.M. van der Veen, O.-H. Kwon, A. Tissot, A. Hauser, A.H. Zewail, Single-nanoparticle phase transitions visualized by four-dimensional electron microscopy, *Nat. Chem.* 5 (2013) 395–402, <https://doi.org/10.1038/NCHEM.1622>.
- [14] K. Sun, S.S. Sun, C. Zhu, H.F. Tian, H.X. Yang, J.Q. Li, Hidden cdw states and insulator-to-metal transition after a pulsed femtosecond laser excitation in layered chalcogenide 1T-TaS_{2-x}Se_x, *Sci. Adv.* 4 (2018) eaas9660, <https://doi.org/10.1126/sciadv.aas9660>.
- [15] D.J. Flannigan, P.C. Samartzis, A. Yurtsever, A.H. Zewail, Nanomechanical motions of cantilevers: direct imaging in real space and time with 4D electron microscopy, *Nano Lett* 9 (2009) 875–881, <https://doi.org/10.1021/nl803770e>.
- [16] T. Eggebrecht, M. Möller, J.G. Gatzmann, N.R. da Silva, A. Feist, U. Martens, H. Ulrichs, M. Münzenberg, C. Ropers, S. Schäfer, Light-induced metastable magnetic texture uncovered by in situ Lorentz microscopy, *Phys. Rev. Lett.* 118 (2017) 097203, <https://doi.org/10.1103/PhysRevLett.118.097203>.
- [17] N.R. da Silva, M. Möller, A. Feist, H. Ulrichs, C. Ropers, S. Schäfer, Nanoscale mapping of ultrafast magnetization dynamics with femtosecond Lorentz microscopy, *Phys. Rev. X* 8 (2018) 031052, <https://doi.org/10.1103/PhysRevX.8.031052>.
- [18] G. Berruto, I. Madan, Y. Murooka, G.M. Vanacore, E. Pomarico, J. Rajeswari, R. Lamb, P. Huang, A.J. Kruckhov, Y. Togawa, T. LaGrange, D. McGrouther, H.M. Rønnow, F. Carbone, Laser-induced skyrmion writing and erasing in an ultrafast cryo-Lorentz transmission electron microscope, *Phys. Rev. Lett* 120 (2018) 117201, <https://doi.org/10.1103/PhysRevLett.120.117201>.
- [19] F. Carbone, B. Barwick, O.-H. Kwon, H.S. Park, J.S. Baskin, A.H. Zewail, EELS femtosecond resolved in 4D ultrafast electron microscopy, *Chem. Phys. Lett.* 468 (2009) 107–111, <https://doi.org/10.1016/j.cplett.2008.12.027>.
- [20] L. Piazza, C. Ma, H.X. Yang, A. Mann, Y. Zhu, J.Q. Li, F. Carbone, Ultrafast structural and electronic dynamics of the metallic phase in a layered manganite, *Struct. Dyn.* 1 (2014) 014501, <https://doi.org/10.1063/1.4835116>.
- [21] F. Carbone, Dynamics deep from the core, *Struct. Dyn.* 2 (2015) 020601, <https://doi.org/10.1063/1.4918727>.
- [22] B. Barwick, D.J. Flannigan, A.H. Zewail, Photon-induced near-field electron microscopy, *Nature* 462 (2009) 902–906, <https://doi.org/10.1038/nature08662>.
- [23] H. Liu, J.S. Baskin, A.H. Zewail, Infrared PINEM developed by diffraction in 4D UEM, *PNAS* 113 (2016) 2041–2046, <https://doi.org/10.1073/pnas.1600317113>.
- [24] L. Piazza, T.T.A. Lummen, E. Quiñonez, Y. Murooka, B.W. Reed, B. Barwick, F. Carbone, Simultaneous observation of the quantization and the interference pattern of a plasmonic near-field, *Nat. Commun.* 6 (2015) 6407, <https://doi.org/10.1038/ncomms7407>.
- [25] T.T.A. Lummen, R.J. Lamb, G. Berruto, T. LaGrange, L.D. Negro, F.J.G. de Abajo, D. McGrouther, B. Barwick, F. Carbone, Imaging and controlling plasmonic interference fields at buried interfaces, *Nat. Commun.* 7 (2016) 13156, <https://doi.org/10.1038/ncomms13156>.
- [26] D.A. Plemmons, P.K. Suri, D.J. Flannigan, Probing structural and electronic dynamics with ultrafast electron microscopy, *Chem. Mater.* 27 (2015) 3178–3192, <https://doi.org/10.1021/acs.chemmater.5b00433>.
- [27] D.B. Williams, C.B. Carter, *Transmission Electron Microscopy-A Textbook for Materials Science*, Springer, 1996, https://doi.org/10.1007/978-1-4757-2519-3_1.
- [28] T. LaGrange, G.H. Campbell, B.W. Reed, M. Taheri, J.B. Pesavento, J.S. Kim, N.D. Browning, Nanosecond time-resolved investigations using the in situ dynamic transmission electron microscope (DTEM), *Ultramicroscopy* 108 (2008) 1441–1449, <https://doi.org/10.1016/j.ultramic.2008.03.013>.
- [29] B.W. Reed, T. LaGrange, R.M. Shuttlesworth, D.J. Gibson, G.H. Campbell, N.D. Browning, Solving the accelerator-condenser coupling problem in a nanosecond dynamic transmission electron microscope, *Rev. Sci. Instrum.* 81 (2010) 053706, <https://doi.org/10.1063/1.3427234>.
- [30] D.A. Plemmons, D.J. Flannigan, Ultrafast electron microscopy: instrument response from the single-electron to high bunch-charge regimes, *Chem. Phys. Lett.* 683 (2017) 186–192, <https://doi.org/10.1016/j.cplett.2017.01.055>.
- [31] K. Bücker, M. Picher, O. Crégut, T. LaGrange, B.W. Reed, S.T. Park, D.J. Masiel, F. Banhart, Electron beam dynamics in an ultrafast transmission electron microscope with Wehnelt electrode, *Ultramicroscopy* 171 (2016) 8–18, <https://doi.org/10.1016/j.ultramic.2016.08.014>.
- [32] Y.M. Lee, Y.J. Kim, Y.-J. Kim, O.-H. Kwon, Ultrafast electron microscopy integrated with a direct electron detection camera, *Struct. Dyn.* 4 (2017) 044023, <https://doi.org/10.1063/1.4983226>.
- [33] S. Ji, L. Piazza, G. Cao, S.T. Park, B.W. Reed, D.J. Masiel, J. Weissenrieder, Influence of cathode geometry on electron dynamics in an ultrafast electron microscope, *Struct. Dyn.* 4 (2017) 054303, <https://doi.org/10.1063/1.4994004>.
- [34] L. Piazza, D.J. Masiel, T. LaGrange, B.W. Reed, B. Barwick, F. Carbone, Design and implementation of a fs-resolved transmission electron microscope based on thermionic gun technology, *Chem. Phys.* 423 (2013) 79–84, <https://doi.org/10.1016/j.chemphys.2013.06.026>.
- [35] A. Feist, N. Bach, N.R. da Silva, T. Danz, M. Möller, K.E. Priebe, T. Domröse, J.G. Gatzmann, S. Rost, J. Schauss, S. Strauch, R. Bormann, M. Sivils, S. Schäfer, C. Ropers, Ultrafast transmission electron microscopy using a laser-driven field emitter: femtosecond resolution with a high coherence electron beam, *Ultramicroscopy* 176 (2017) 63–73, <https://doi.org/10.1016/j.ultramic.2016.12.005>.
- [36] N. Bach, T. Domröse, A. Feist, T. Rittmann, S. Strauch, C. Ropers, S. Schäfer, Coulomb interactions in high-coherence femtosecond electron pulses from tip emitters, *Struct. Dyn.* 6 (2019) 014301, <https://doi.org/10.1063/1.5066093>.
- [37] G.M. Caruso, F. Houdellier, P. Abeilhou, A. Arbouet, Development of an ultrafast electron source based on a cold-field emission gun for ultrafast coherent TEM, *Appl. Phys. Lett.* 111 (2017) 023101, <https://doi.org/10.1063/1.4991681>.
- [38] F. Houdellier, G.M. Caruso, S. Weber, M. Kociak, A. Arbouet, Development of a high brightness ultrafast transmission electron microscope based on a laser-driven cold field emission source, *Ultramicroscopy* 186 (2018) 128–138, <https://doi.org/10.1016/j.ultramic.2017.12.015>.
- [39] H. Dömer, O. Bostanjoglo, High-speed transmission electron microscope, *Rev. Sci. Instrum.* 74 (2003) 4369, <https://doi.org/10.1063/1.1611612>.
- [40] V.A. Lobastov, R. Srinivasan, A.H. Zewail, Four-dimensional ultrafast electron microscopy, *PNAS* 102 (2005) 7069–7073, <https://doi.org/10.1073/pnas.0502607102>.
- [41] T. LaGrange, M.R. Armstrong, K. Boyden, C.G. Brown, G.H. Campbell, J.D. Colvin, W.J. DeHope, A.M. Frank, D.J. Gibson, F.V. Hartemann, J.S. Kim, W.E. King, B.J. Pyke, B.W. Reed, M.D. Shirk, R.M. Shuttlesworth, B.C. Stuart, B.R. Torralva, Single-shot dynamic transmission electron microscopy, *Appl. Phys. Lett.* 89 (2006) 044105, <https://doi.org/10.1063/1.2236263>.
- [42] R. Bormann, S. Strauch, S. Schäfer, C. Ropers, An ultrafast electron microscope gun driven by two-photon photoemission from a nanotip cathode, *J. Appl. Phys.* 118 (2015) 173105, <https://doi.org/10.1063/1.4934681>.
- [43] S.T. Park, M. Lin, A.H. Zewail, Photon-induced near-field electron microscopy (PINEM): theoretical and experimental, *New J. Phys.* 12 (2010) 123028, <https://doi.org/10.1088/1367-2630/12/12/123028>.
- [44] S. McVitie, M. Cushley, Quantitative Fresnel Lorentz microscopy and the transport of intensity equation, *Ultramicroscopy* 106 (2006) 423–431, <https://doi.org/10.1016/j.ultramic.2005.12.001>.
- [45] X.Z. Yu, Y. Onose, N. Kanazawa, J.H. Park, J.H. Han, Y. Matsui, N. Nagaosa, Y. Tokura, Real-space observation of a two-dimensional skyrmion crystal, *Nature* 465 (2010) 901–904, <https://doi.org/10.1038/nature09124>.
- [46] J.C. Loudon, S. Yazdi, T. Kasama, N.D. Zhigadlo, J. Karpinski, Measurement of the penetration depth and coherence length of MgB₂ in all directions using transmission electron microscopy, *Phys. Rev. B* 91 (2015) 054505, <https://doi.org/10.1103/PhysRevB.91.054505>.
- [47] S.A. Hilbert, A. Neukirch, C.J.G.J. Uiterwaal, H. Batelaan, Exploring temporal and rate limits of laser-induced electron emission, *J. Phys. B* 42 (2009) 141001, <https://doi.org/10.1088/0953-4075/42/14/141001>.